Supplement of Biogeosciences, 23, 995–1012, 2026
https://doi.org/10.5194/bg-23-995-2026-supplement
© Author(s) 2026. CC BY 4.0 License.

Biogeosciences Open Access EGU

Supplement of

Perturbation increases source-dependent organic matter degradation rates in estuarine sediments

Guangnan Wu et al.

Correspondence to: Guangnan Wu (guangnan.wu@nioz.nl)

The copyright of individual parts of the supplement might differ from the article licence.

23
24

TABLE OF CONTENTS Page

25
26
27
28
29
30
31

Table. S1. Composition of artificial rainwater used in aerobic incubation experiments for moisture adjustment. The composition was based on the Dutch rainwater (Harpenslager et al., 2015). Chemicals were analytical grade dissolved in milli-Q water.

Salt	Concentration (mg/L)
NaCl	3.13
$MgSO_4 \cdot 7H_2O$	1.91
$MgCl_2 \cdot 6H_2O$	1.22
$CaCl_2 \cdot H_2O$	2.58
KCl	1.61

Determination of homogenized freeze-dried sediment bulk density and porosity

Bulk density was measured based on the method described in Al-Shammary et al. (2018). Homogenized freeze-dried sediment was carefully poured into a pre-weighed 50-mL graduated cylinder. The cylinder was gently tapped to level the sediment surface at 50-mL mark. The mass (m_{dry}) and the volume (V_{dry}, here 50 mL) of the freeze-dried sediment were then recorded. Bulk density (ρ_{bulk}) was calculated as:

$$\rho_{bulk} = \frac{m_{dry}}{V_{dry}}$$

The sediment particle density (ρ_{sed}) was assumed to be 2.65 g cm^{-3}. Porosity (ø) was calculated according to:

$$ø = 1 - \frac{\rho_{bulk}}{\rho_{sed}}$$

The required volume of artificial rainwater (V_{water}) to adjust water-filled pore space to 60% for 10 g of homogenized freeze-dried sediment was calculated as:

$$V_{water} = \frac{10\ grams}{\rho_{sed}} \cdot ø \cdot 60\%$$

Homogenized freeze-dried sediment bulk density (ρ_{bulk}) and porosity (ø) were 0.92 g cm^{-3} and 0.65 for site 115, 0.72 g cm^{-3} and 0.73 for site 86, 1.36 g cm^{-3} and 0.49 for site NWWG-02, 0.91 g cm^{-3} and 0.66 for site 21A, 0.81 g cm^{-3} and 0.69 for site B16, 1.31 g cm^{-3} and 0.51 for site K1v2.

Table S2. MixSIAR modelled marine, riverine, and terrestrial contributions to the OM in 49 PoR sediments, respectively. Mean value and standard deviation are provided.

Sediment site	Marine contribution	Riverine contribution	Terrestrial contribution
201	45% ± 19.6%	32.7% ± 19.8%	22.3% ± 19.1%
130	49.9% ± 19.7%	28% ± 18%	22% ± 18.9%
93	27.5% ± 16.5%	36.3% ± 22%	36.2% ± 23.3%
131	58.1% ± 19.4%	23.7% ± 16.3%	18.2% ± 17.3%
202	41.5% ± 19%	21.7% ± 16.1%	36.8% ± 22.3%
117	49% ± 20.1%	32.4% ± 19.6%	18.7% ± 17.8%
90	50.5% ± 20%	28.3% ± 18.3%	21.3% ± 18.6%
89	58.4% ± 19.7%	24.8% ± 16.6%	16.9% ± 17.1%
94	55.5% ± 19.7%	25.8% ± 16.9%	18.7% ± 17.5%
123v1	42.6% ± 19.7%	36% ± 20.7%	21.4% ± 18.7%
115	57.4% ± 19.7%	26.3% ± 17.3%	16.3% ± 16.2%
140	63.4% ± 18.9%	19.8% ± 14.2%	16.8% ± 16.5%
114	62.2% ± 19.2%	22% ± 15.5%	15.8% ± 16.6%
204	32.6% ± 17.7%	34.6% ± 21%	32.8% ± 22.5%
86	63.6% ± 18.7%	20.3% ± 14.6%	16.1% ± 16%
C1	62.7% ± 19.2%	21.4% ± 15.2%	15.9% ± 16.3%
NWWG-09	22.9% ± 16.1%	48.4% ± 24.6%	28.8% ± 22.6%
73	37.3% ± 20.1%	42% ± 22.4%	20.7% ± 19.1%
76	33.8% ± 18.7%	41.1% ± 22.2%	25% ± 20.6%
80C	33.8% ± 18.9%	42.5% ± 22.7%	23.6% ± 20%
71	36.3% ± 19.4%	41.5% ± 22.4%	22.2% ± 19.8%
68	35% ± 19.3%	42.4% ± 22.6%	22.5% ± 20%
66	32.8% ± 18.6%	43.3% ± 22.9%	23.9% ± 20.1%
510	29.1% ± 18.3%	47.3% ± 23.7%	23.6% ± 20.6%
D1	22.5% ± 15.9%	48.2% ± 24.6%	29.3% ± 22.6%
56	32.5% ± 19%	45.6% ± 23.3%	22% ± 19.8%
51	34.6% ± 19.1%	41.2% ± 22.5%	24.2% ± 20.3%
31	31% ± 18.6%	46.3% ± 23.7%	22.7% ± 19.9%
50	26.4% ± 16.3%	37% ± 22.3%	36.7% ± 23.4%
34	27.6% ± 17.7%	47.4% ± 23.9%	25.1% ± 21%
K17	16.9% ± 12.9%	42.8% ± 24.4%	40.3% ± 24.8%
37	17% ± 13.7%	48.9% ± 25.4%	34.1% ± 24.2%
36	22% ± 15.7%	49.2% ± 24.7%	28.8% ± 22.7%
23	18.2% ± 15.4%	59.4% ± 25.4%	22.4% ± 20.9%
21A	24.7% ± 17%	51.2% ± 24.2%	24.1% ± 20.6%
S1	22.5% ± 16.1%	48.5% ± 24.5%	29% ± 22.6%
21Lv2	18.1% ± 15%	56.9% ± 25.4%	24.9% ± 21.5%
17	19.4% ± 14.6%	47.7% ± 24.8%	32.9% ± 23.7%
16	13.2% ± 10.5%	30.6% ± 21.5%	56.2% ± 24.2%
33	13.5% ± 10.8%	33.3% ± 22.5%	53.3% ± 24.6%

B16	13.8% ± 12.7%	55.4% ± 26.3%	30.8% ± 24.2%
B22	14.6% ± 13.2%	55.6% ± 25.8%	29.7% ± 23.6%
NWWG-02	55.9% ± 19.8%	27.3% ± 17.8%	16.8% ± 17.1%
NWWG-16	27.8% ± 17.2%	40.3% ± 22.9%	31.9% ± 22.8%
H4	21% ± 15.6%	48.6% ± 24.8%	30.5% ± 23.2%
84	10.8% ± 9.2%	30.3% ± 21.6%	58.9% ± 23.7%
NMS-18	23.3% ± 15.3%	38.2% ± 22.8%	38.4% ± 24%
14A	17.3% ± 13%	43.6% ± 24.5%	39.1% ± 24.6%
K1v2	24.8% ± 15.8%	12.4% ± 11.5%	62.8% ± 21.1%

Table. S3. Identified pyrolysis products, retention time, and their two fragment ions used to quantify and their assignment according to (Nierop et al., 2017). Types: Alk = *n*-alkenes/alkanes, Ar = aromatics or alkylbenzenes, Gua = guaiacols, Nt = N-containing compounds, Ph = phenols, Phy = phytadienes, Pri = pris-1-ene, Ps = polysaccharide-derived products, Syr = syringols. RT = retention time

RT	Pyrolysis product	*m/z*	Correction factor	Type
9.47	$C_{11:1}$	55+57	4.90	Alk
9.70	$C_{11:0}$	55+57	2.90	Alk
11.50	$C_{12:1}$	55+57	4.90	Alk
11.76	$C_{12:0}$	55+57	2.90	Alk
13.50	$C_{13:1}$	55+57	4.90	Alk
13.72	$C_{13:0}$	55+57	2.90	Alk
15.45	$C_{14:1}$	55+57	4.90	Alk
15.57	$C_{14:0}$	55+57	2.90	Alk
17.15	$C_{15:1}$	55+57	4.90	Alk
17.32	$C_{15:0}$	55+57	2.90	Alk
18.82	$C_{16:1}$	55+57	4.90	Alk
18.98	$C_{16:0}$	55+57	2.90	Alk
20.40	$C_{17:1}$	55+57	4.90	Alk
20.55	$C_{17:0}$	55+57	2.90	Alk
21.90	$C_{18:1}$	55+57	4.90	Alk
22.05	$C_{18:0}$	55+57	2.90	Alk
23.30	$C_{19:1}$	55+57	4.90	Alk
23.48	$C_{19:0}$	55+57	2.90	Alk
24.70	$C_{20:1}$	55+57	4.90	Alk
24.82	$C_{20:0}$	55+57	2.90	Alk
26.00	$C_{21:1}$	55+57	4.90	Alk
26.12	$C_{21:0}$	55+57	2.90	Alk
27.26	$C_{22:1}$	55+57	4.90	Alk
27.36	$C_{22:0}$	55+57	2.90	Alk
28.45	$C_{23:1}$	55+57	4.90	Alk
28.55	$C_{23:0}$	55+57	2.90	Alk
29.59	$C_{24:1}$	55+57	4.90	Alk
29.69	$C_{24:0}$	55+57	2.90	Alk
30.69	$C_{25:1}$	55+57	4.90	Alk
30.79	$C_{25:0}$	55+57	2.90	Alk
31.75	$C_{26:1}$	55+57	4.90	Alk
31.85	$C_{26:0}$	55+57	2.90	Alk
32.76	$C_{27:1}$	55+57	4.90	Alk
32.86	$C_{27:0}$	55+57	2.90	Alk
33.74	$C_{28:1}$	55+57	4.90	Alk
33.84	$C_{28:0}$	55+57	2.90	Alk
34.69	$C_{29:1}$	55+57	4.90	Alk

34.79	$C_{29:0}$	55+57	2.90	Alk
35.60	$C_{30:1}$	55+57	4.90	Alk
35.71	$C_{30:0}$	55+57	2.90	Alk
36.51	$C_{31:1}$	55+57	4.90	Alk
36.60	$C_{31:0}$	55+57	2.90	Alk
1.84	Benzene	78	1.90	Ar
2.97	Toluene	91+92	1.37	Ar
4.50	Ethylbenzene	91+106	1.60	Ar
4.68	1,3- and 1,4-Dimethylbenzene	91+106	1.60	Ar
5.01	Styrene	103+104	2.06	Ar
5.10	1,2-Dimethylbenzene	91+106	1.60	Ar
9.02	Guaiacol	109+124	1.92	Gua
11.21	4-Methylguaiacol	123+138	2.37	Gua
12.92	4-Ethylguaiacol	137+152	1.24	Gua
13.57	4-Vinylguaiacol	135+150	2.37	Gua
14.39	Eugenol	149+164	4.19	Gua
15.33	*cis*-Isoeugenol	149+164	4.19	Gua
16.06	*trans*-Isoeugenol	149+164	4.19	Gua
16.58	4-Acetylguaiacol	151+166	4.12	Gua
2.53	Pyridine	52+79	1.97	Nt
2.69	Pyrrole	67	1.67	Nt
3.98	2-Methylpyrrole	80+81	1.54	Nt
4.19	3-Methylpyrrole	80+81	1.54	Nt
4.36	4-Methylpyridine	66+93	1.93	Nt
9.67	Benzyl nitrile	90+117	2.38	Nt
11.68	Methylbenzylnitril	91+131	2.24	Nt
13.11	Indole	90+117	2.05	Nt
14.85	Methylindole	130+131	2.73	Nt
20.05	Diketodipyrrole	93+186	3.21	Nt
21.64	Diketopiperazine	70+154	5.20	Nt
23.20	Diketopiperazine	70+194	5.20	Nt
23.22	Diketopiperazine	70+154	5.20	Nt
7.17	Phenol	66+94	1.72	Ph
8.62	2-Methylphenol	107+108	2.93	Ph
9.10	3/4-Methylphenol	107+108	2.35	Ph
10.95	4-Ethylphenol	107+122	1.76	Ph
12.04	4-Vinylphenol	91+120	1.78	Ph
12.13	Catechol	64+110	2.42	Ph
22.58	Neophytadiene	68+82	5.79	Phy
22.91	*cis*-1,3-Phytadiene	68+82	6.80	Phy
23.19	*trans*-1,3-Phytadiene	68+82	6.80	Phy
21.02	Prist-1-ene	56+57	3.44	Pri
3.75	2-Furaldehyde	95+96	1.60	Ps

6.20	5-Methyl-2-furaldehyde	109+110	1.80	Ps
6.93	4-Hydroxy-5,6-dihydro-(2H)-pyran-2-one	58+114	1.60	Ps
9.02	Levoglucosenone	96+98	4.59	Ps
17.81	Levoglucosan	60+73	2.10	Ps
14.14	Syringol	139+154	2.38	Syr
15.93	4-Methylsyringol	153+168	2.94	Syr
17.32	4-Ethylsyringol	167+182	1.28	Syr
17.94	4-Vinylsyringol	165+180	3.03	Syr
18.57	4-Allylsyringol	179+194	3.08	Syr
19.37	*cis*-4-Prop-2-enylsyringol	179+194	3.08	Syr
20.14	*trans*-4-Prop-2-enylsyringol	179+194	3.08	Syr
20.57	4-Acetylsyringol	181+196	3.90	Syr

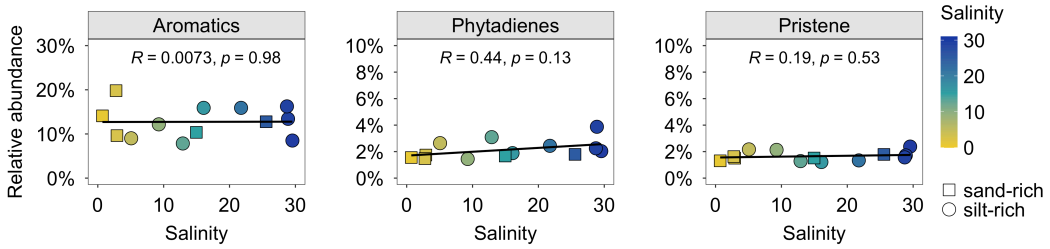

Fig. S1. Relative abundance of aromatics, phytadienes, and prist-1-ene in MOM pyrolysis products.

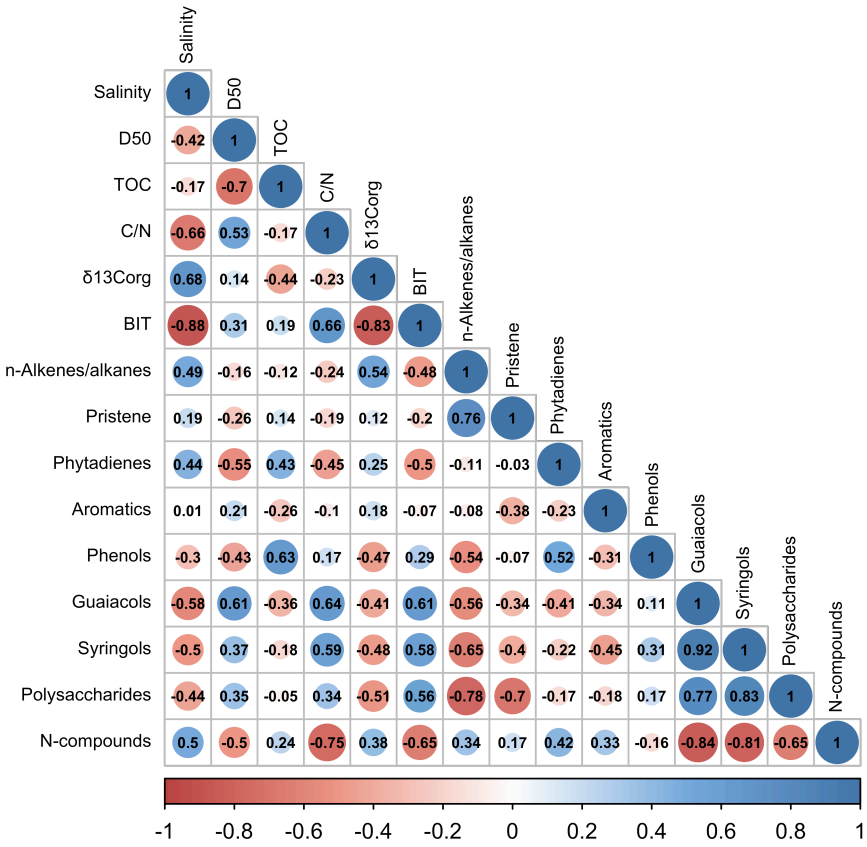

Fig. S2. The Pearson's correlation matrix of major sediment properties (i.e. salinity, D50, TOC) with sediment OM source proxies (i.e. CN, BIT index, and MOM pyrolysis products).

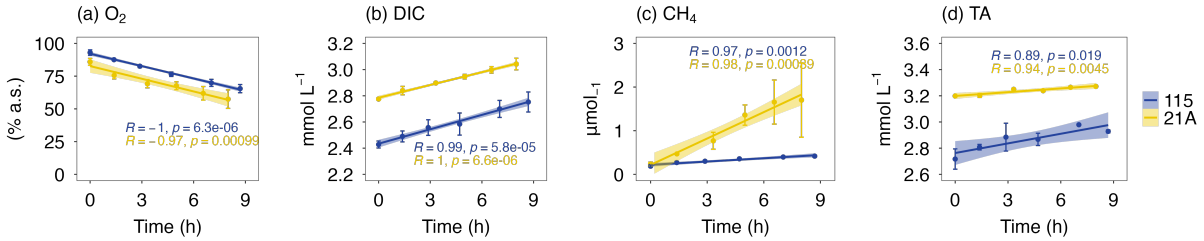

Fig. S3. The concentration of dissolved O_2, DIC, CH_4 and TA in the overlaying water over time during intact sediment core incubation.

Estimation of contribution by OM degradation to sedimentary DIC efflux

We correct the measured total DIC fluxes, calculated from time series shown in Fig. S3, for sources other than oxic and anaerobic OM degradation, e.g. $CaCO_3$ dissolution. In our approach, we consider sulfate reduction, estimated from benthic sulfate diffusive rate, and $CaCO_3$ dissolution as the main total alkalinity (TA) sources with DIC:TA ratios of 1:1 and 2:1, respectively. The SO_4^{2-}:TA stoichiometry of sulfate reduction is assumed to be 1:2, the theoretical ideal stoichiometry that has also been found experimentally in organic-rich coastal sediment (Burdige, 2012; Rassmann et al., 2020). Note that aerobic OM degradation does not contribute to TA. Porewater data indicated that other anaerobic OM degradation pathways (e.g. Fe-(oxyhydr)oxides reduction, methanogenesis) were minor compared to sulfate reduction in the surface sediment, thus not considered in the DIC_{OM} calculation.

Here, we assume that the diffusive sulfate flux across the sediment-water interface represents the sulfate reduction rate in the uppermost sediment that contributes to the TA and DIC efflux. Sulfate reduction in the uppermost sediment is assumed to arise from organoclastic sulfate reduction (not e.g. CH_4 oxidation) and therefore contributes to DIC production from OM degradation (Jørgensen, 2021). Sulfate diffusive fluxes were calculated from the measured sulfate concentration gradients between the bottom water and porewater in the uppermost sediment (0–0.5 cm, average 0.25 cm below sediment-water interface; Table S4) using Fick's first law:

$$J = -\varphi \times D_{sed} \times \frac{dC}{dz}$$

where J is the diffusive flux (mmol m^{-2} d^{-1}), D_{sed} is the diffusion coefficient in sediment (m^2 d^{-1}) and dC/dz is the concentration gradient at the sediment-water interface (mol m^{-4}). The RStudio package '*marelac*' (Soetaert et al., 2023) was used to calculate sulfate diffusion coefficients in water (D_w) for site 115 (salinity 29) and 21A (salinity 5). The temperature applied in the equation was 19 °C as measured during field work in summer 2021. To calculate the D_{sed} from the diffusion coefficient in water (D_w) porosity of 0.95 was used for the uppermost fine-grained sediment at both locations to correct for the tortuosity effect:

$$D_{sed} = \frac{D_w}{1 - 2 \times \log(porosity)}$$

Table S4. Key parameters for calculation of diffusive sulfate fluxes in the surface sediment.

Site	Species	BW	Sed (0.25 cm)	D_{sed} (m^2 d^{-1})	J_{SO4} (mmol m^{-2} d^{-1})
115 (marine)	SO_4^{2-}	25.0 mM	23.9 mM	6.85e−5	−28.6
21A (riverine)	SO_4^{2-}	4.5 mM	3.9 mM	7.2e−5	−16.4

The TA flux from sulfate reduction was obtained by multiplying the SO_4^{2-} flux by a factor of 2 (SO_4^{2-}:TA of the reaction is 1:2). Assuming that the remaining TA flux can be ascribed to $CaCO_3$ dissolution, the corrected alkalinity flux was then used to estimate DIC efflux from $CaCO_3$ dissolution (TA:DIC of $CaCO_3$ dissolution is 2:1). The DIC_{CaCO3} was then used to calculate the OM-derived DIC flux, DIC_{OM} (Table S5).

Table S5. Simplified mass balance for benthic DIC and TA fluxes at sites 115 and 21A. $f_{DIC\text{-}OM}$ represents the fraction of the DIC efflux that can be attributed to OM degradation.

Site	DIC	TA	TA_{SO4}	DIC_{CaCO3}	DIC_{OM}	$f_{DIC\text{-}OM}$
	(mmol m^{-2} d^{-1})					na
115 (marine)	158±52	96±28	57.2	20±14	139±53	0.88±0.4
21A (riverine)	122± 27	41±8	32.8	4±4	118±27	0.97±0.3

The relatively low contribution of $CaCO_3$ dissolution to DIC efflux, 3–12 %, aligns with previous work that emphasizes the dominant role of OM degradation in DIC fluxes from (organic-rich) non-carbonate coastal sediment (Krumins et al., 2013).

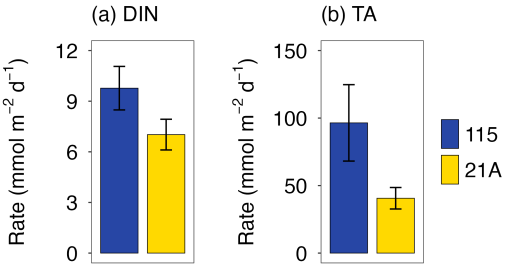

Fig. S4. Benthic fluxes of (a) dissolved inorganic nitrogen (DIN) and (b) total alkalinity (TA) determined from whole-core incubation. Error bars represent the standard deviation from triplicate core incubations.

Benthic diffusive fluxes of Fe^{2+} and HS^-

Diffusion fluxes of Fe^{2+} and HS^- were calculated the same way as SO_4^{2-} diffusing fluxes using Fick's first law. Table S6 presents key data for the calculation.

Table. S6 Benthic diffusive fluxes of Fe^{2+} and HS^- for sediment 115 and 21A.

Site	Species	BW	Sed (0.25 cm)	D_{sed} (m^2 d^{-1})	J (mmol m^{-2} d^{-1})
115 (marine)	Fe^{2+}	0.25 μM	2.7 μM	4.54e−5	0.04
21A (riverine)	Fe^{2+}	0.24 μM	0.87 μM	4.78e−5	0.01
115 (marine)	HS^-	0 mM	0 mM	1.16e−4	0
21A (riverine)	HS^-	0.003 mM	0.004 mM	1.22e−4	0.05

$$4Fe^{2+} + O_2 + 10H_2O \rightarrow 4Fe(OH)_3 + 8H^+$$

$$HS^- + 2O_2 \rightarrow SO_4^{2-} + H^+$$

Assuming all upward diffusing fluxes of Fe^{2+} and HS^- were completely oxidized by O_2, the oxidation rates were ~ 0.1 mmol m^{-2} d^{-1} for both site 115 and 21A, which contributed to less than 1% of the total O_2 consumption rates for both sites.

References

Al-Shammary, A. A. G., Kouzani, A. Z., Kaynak, A., Khoo, S. Y., Norton, M., and Gates, W.: Soil Bulk Density Estimation Methods: A Review, Pedosphere, 28, 581–596, https://doi.org/10.1016/s1002-0160(18)60034-7, 2018.

Burdige, D. J.: Estuarine and Coastal Sediments - Coupled Biogeochemical Cycling, Elsevier Inc., 279–316 pp., https://doi.org/10.1016/B978-0-12-374711-2.00511-8, 2012.

Harpenslager, S. F., Van Dijk, G., Kosten, S., Roelofs, J. G. M., Smolders, A. J. P., and Lamers, L. P. M.: Simultaneous high C fixation and high C emissions in Sphagnum mires, Biogeosciences, 12, 4739–4749, https://doi.org/10.5194/bg-12-4739-2015, 2015.

Jørgensen, B. B.: Sulfur Biogeochemical Cycle of Marine Sediments, Geochem Perspect, 10, 145–303, https://doi.org/10.7185/GEOCHEMPERSP.10.2, 2021.

Krumins, V., Gehlen, M., Arndt, S., Van Cappellen, P., and Regnier, P.: Dissolved inorganic carbon and alkalinity fluxes from coastal marine sediments: Model estimates for different shelf environments and sensitivity to global change, Biogeosciences, 10, 371–398, https://doi.org/10.5194/bg-10-371-2013, 2013.

Nierop, K. G. J., Reichart, G. J., Veld, H., and Sinninghe Damsté, J. S.: The influence of oxygen exposure time on the composition of macromolecular organic matter as revealed by surface sediments on the Murray Ridge (Arabian Sea), Geochim Cosmochim Acta, 206, 40–56, https://doi.org/10.1016/j.gca.2017.02.032, 2017.

Rassmann, J., Eitel, E. M., Lansard, B., Cathalot, C., Brandily, C., Taillefert, M., and Rabouille, C.: Benthic alkalinity and dissolved inorganic carbon fluxes in the Rhône River prodelta generated by decoupled aerobic and anaerobic processes, Biogeosciences, 17, 13–33, https://doi.org/10.5194/bg-17-13-2020, 2020.

Soetaert, K., Petzoldt, T., Meysman, F., and Meire, L.: marelac: Tools for Aquatic Sciences, 2023.